The Effects of Ocean Surface Waves on Global Intraseasonal Prediction: Case Studies with a Coupled CFSv2.0-WW3 System

Ruizi Shi[1], Fanghua Xu[1*], Li Liu[1], Zheng Fan[1], Hao Yu[1], Hong Li[1,3], Xiang Li[2] and Yunfei Zhang[2]

[1] Ministry of Education Key Laboratory for Earth System Modeling, and Department of Earth System Science, Tsinghua University, Beijing, 100084, China

[2] Key Laboratory of Marine Hazards Forecasting, National Marine Environmental Forecasting Center, Ministry of Natural Resources, Beijing, 100081, China

[3] Department of Atmospheric and Oceanic Sciences and Institute of Atmospheric Sciences, Fudan University, Shanghai, 200433, China.

Correspondence to: Fanghua Xu (fxu@mail.tsinghua.edu.cn)

Abstract. This article describes the implementation of a coupling between a global forecast model (CFSv2.0) and a wave model (WW3), and investigates the effects of ocean surface waves on the air-sea interface in the new framework. Several major wave-related processes, including the Langmuir mixing, Stokes-Coriolis force with entrainment, air-sea fluxes modified by Stokes drift and momentum roughness length, are evaluated in two groups of 56-day experiments, one for boreal winter and the other for boreal summer. Comparisons are made against in-situ buoys, satellite measurements and reanalysis data, to evaluate the influence of waves on intraseasonal prediction of sea surface temperature (SST), 2-m air temperature (T02), mixed layer depth (MLD), 10-m wind speed (WSP10) and significant wave height (SWH). The wave-coupled experiments show that overestimated SSTs and T02s, as well as underestimated MLDs at mid-high latitudes in summer from original CFSv2.0 are significantly improved due to enhanced vertical mixing generated by Stokes drift. For WSP10s and SWHs, the wave-related processes generally reduce biases in regions where WSP10s and SWHs are overestimated. On one hand, the decreased SSTs stabilize the marine atmospheric boundary layer, weaken WSP10s and then SWHs. On the other hand, the increased roughness length due to waves reduces the originally overestimated WSP10s and SWHs. In addition, the effects of Stokes drift and current on air-sea fluxes also rectify WSP10s and SWHs. These cases are helpful for the future development of the two-way CFSv2.0-wave coupled system.

1 Introduction

Ocean surface gravity waves play an important role in modifying physical processes at the atmosphere-ocean interface, which can influence momentum, heat and freshwater fluxes across the air-sea interface (Li and Garrett, 1997; Taylor and Yelland, 2001; Moon et al., 2004; Janssen 2004; Belcher et al., 2012; Moum and Smyth, 2019). For instance, ocean surface waves modify ocean surface roughness to influence the marine atmospheric boundary layer and thus change the momentum, latent heat, and sensible heat transfer (Janssen 1989, 1991; Taylor and Yelland, 2001; Moon et al., 2004; Drennan et al., 2003, 2005). The breaking waves inject turbulent kinetic energy in the upper ocean, which enhances the mixing process (Terray et al. 1996). Nonbreaking surface waves also affect mixing in the upper ocean by adding a wave-related Reynolds stress (Qiao et al., 2004; Ghantous and Babanin, 2014). The wave-related Stokes drift interacts with Coriolis force and produces the Coriolis-Stokes force (Hasselmann 1970). The shear of Stokes drift is critical for generation of Langmuir circulation, which significantly deepens the mixed layer by strong vertical mixing both at climate scales (Li and Garrett 1997; Belcher et al., 2012) and at weather scales (Kukulka et al., 2009).

Various wave-related parameterizations have been proposed and used in modelling. The wave-related Charnock parameter (C_{ch}) defines sea surface roughness and affects wind stress estimates (Pineau-Guillou et al. 2018; Sauvage et al. 2020). There are primarily three methods for defining C_{ch}, assessed from the wave-induced kinematic stress (Janssen 1989, 1991), the wave age (Drennan et al., 2003, 2005; Moon et al., 2004), or the steepness (Taylor and Yelland, 2001). The former two are based on the wind-sea conditions, whereas the latter includes both swells and wind-sea waves. Modifications to these Charnock parameterizations were suggested in recent studies for the leveling off roughness under high winds (e.g., Fan et al., 2012; Bidlot et al., 2020; ECMWF, 2020; Li et al., 2021). In the oceanic boundary

56   layer, waves influence upper ocean mixing via wave dissipation and Stokes drift-induced processes. In

57   Breivik et al. (2015), the wave dissipation-related turbulent kinetic energy flux is found to yield the

58   largest sea surface temperature (SST) differences in the extratropics. The Stokes drift-induced Langmuir

59   turbulence can improve temperature simulation over most of the world oceans, particularly in the

60   Southern Ocean (Belcher et al., 2012; Li et al., 2016). Polonichko (1997), Van Roekel et al. (2012) and

61   Li et al. (2017) indicated that the Langmuir cell intensity strongly depends on the alignment of winds

62   and waves, reaching maximum when they are aligned. Li et al. (2016) found the effect of Langmuir cell

63   can be further enhanced by entrainment. In Couvelard et al. (2020), the Stokes drift-related forces can

64   also contribute modestly to the deepening of the mixed layer depth (MLD). In the First Institute of

65   Oceanography Earth System Model, Bao et al. (2019) indicated that the non-breaking wave-induced

66   mixing, Stokes drift-affected air-sea fluxes, as well as sea spray are all important for climate estimates.

67   The wave-related processes at the air-sea interface are complex and important in global coupled

68   systems (e.g., Breivik et al. 2015; Law-Chune and Aouf, 2018; Bao et al. 2019; Couvelard et al. 2020).

69   Most of the coupled models with a wave component at global scale were developed for climate research

70   (e.g., Law-Chune and Aouf, 2018; Bao et al. 2019; Couvelard et al. 2020). Exceptionally, an Integrated

71   Forecasting System (IFS) with fully coupled atmosphere, ocean and wave components, developed by

72   European Centre for Medium-Range Weather Forecasts (ECMWF) (Janssen 2004; Bidlot et al. 2019,

73   2020), has been released with great flexibility for global forecasts from medium-range weather scales to

74   seasonal scales (Breivik et al. 2015).

75   The effects of wave-related processes are worth further evaluation in different global coupled

76   modelling systems. Since it takes sufficient periods for the wave energy to develop (Janssen 2004), we

77   investigate the impact of individual wave process at intraseasonal timescale in a new global atmosphere-

78   ocean-wave system. To achieve this, we coupled the WAVEWATCH III (WW3) to the Climate Forecast

79   System model version 2.0 (CFSv2.0) and then conducted sensitivity experiments in boreal winter and

80   summer for comparison. The effects of upper ocean mixing modified by Langmuir cell, Stokes-Coriolis

81   force and entrainment, air-sea fluxes modified by surface current and Stokes drift, and momentum

82   roughness length are evaluated. The CFSv2.0 is a coupled system with the main application for

83   intraseasonal and seasonal prediction (e.g., Saha et al. 2014). The National Centers for Environmental

84   Prediction (NCEP) is establishing its atmosphere-ocean-wave system, in which the Global Forecast

85   System (GFS; the atmosphere module in CFSv2.0 system) is one-way coupled with WW3. Our work can

86   provide insights for two-way wave coupling of CFSv2.0, and is helpful for the future development of the

87   CFSv2.0-wave coupling system. Two groups of 56-day predictions were conducted for boreal winter and

88   boreal summer, respectively. Then, the predictions were compared with observations and reanalysis data.

89   For each group, sensitivity experiments with different wave parameterizations were carried out to

90   evaluate the effects of individual wave-related process.

91   The rest of the paper is structured as follows: methods and numerical experiments with different

92   parameterizations are described in Section 2; the observations and reanalysis data are introduced in

93   Section 3, and the results of experiments are evaluated and compared in Section 4. Finally, a summary

94   and discussion are given in Section 5.

95   **2 Methods and Experiments**

96   **2.1 Coupling WAVEWATCH III with CFSv2.0**

97   The version 5.16 of WW3 (WAVEWATCH III Development Group, 2016) developed by the National

98   Oceanic and Atmospheric Administration (NOAA)/NCEP has been incorporated into the CFSv2.0 (Saha

99   et al., 2014) as a new model component. The latitude range of WW3 is 78°S-78°N with a spatial

100   resolution of 1/3°; the frequency range is 0.04118-0.4056Hz and the total number of frequencies is 25;

101   the number of wave directions is 24 with a resolution of 15°; the maximum global time step and the

102   minimum source term time step are both 180 s.

103   The CFSv2.0 contains two components, the GFS (details are available at

104   http://www.emc.ncep.noaa.gov/GFS/doc.php) as the atmosphere component and the Modular Ocean

105   Model version 4 (MOM4; Griffies et al., 2004) as the ocean component. The MOM4 is integrated on a

106   nominal 0.5° horizontal grid with the enhanced horizontal resolution to 0.25° in the tropics, and has 40

107   vertical levels; the vertical spacing is 10 m in the upper 225 m, and then increases in unequal intervals to

108   the bottom at 4478.5 m. A three-layer sea ice model is included in MOM4 (Wu et al. 2005). The GFS

109   uses a spectral triangular truncation of 382 waves (T382) in the horizontal, which is equivalent to a grid

110   resolution of nearly 35 km, and 64 sigma-pressure hybrid layers in the vertical. The time steps of both

111   MOM4 and GFS are 180 s. The ocean and atmosphere components are then coupled at the same rate. In

112   the original two-way coupled system, the GFS receives SST from MOM4 and sends fluxes of heat,

113   momentum, freshwater to MOM4 (black arrows in Fig. 1).

114   The Chinese Community Coupler version 2.0 (C-Coupler2; Liu et al., 2018) is used to interpolate and

115   pass variables between atmosphere and wave components as well as ocean and wave components. Each

116   component receives inputs and supplies outputs on its own grids. The C-Coupler2 is a common, flexible

117   and user-friendly coupler, which contains a dynamic 3-D coupling system and enables variables to remain

118   conserved after interpolation.

119   A schematic diagram of the coupled atmosphere-ocean-wave system is shown in Fig. 1. As illustrated,

120   WW3 is two-way coupled with MOM4 and GFS, through the C-Coupler2. WW3 is forced by 10-m wind

121   from GFS (green arrows) and surface current from MOM4 (blue arrows), and then generates and evolves

122   the wave action density spectrum. Meanwhile, the surface Stokes drift velocity, the Stokes transport and

123   the turbulent Langmuir number are passed to MOM4 (red arrows; see Section 2.3) from WW3, and the

124   surface Stokes drift velocity and the Charnock parameter are passed to GFS (red arrows; see Section 2.4

125   and 2.5). The high frequency tail assumption for Stokes drift in WW3 is used with a spectral level

126   decaying as f^{-5} (frequency). Additionally, the regular ocean surface current velocities from MOM4 are

127   also passed to GFS, to calculate the relative wind velocity for the turbulent fluxes together with surface

128   Stokes drift (blue arrows; see Section 2.4).

129   Both the CFSv2.0 and WW3 use warm starts; the initial fields at 00:00 UTC of the first day in each

130   experiment for CFSv2.0 were generated by the real time operational Climate Data Assimilation System

131   (Kalnay et al., 1996), downloaded from the CFSv2.0 official website

132   (http://nomads.ncep.noaa.gov/pub/data/nccf/com/cfs/prod). To get initial conditions for WW3, a stand-

133   alone WW3 model is set up synchronously (see Section 2.2). Since the interactions between waves and

134   sea ice are complicated and beyond the scope of the study, we turn off the coupling between WW3 and

135   CFSv2.0 in areas with sea ice.

136   In addition, to properly select the coupling frequency between CFSv2.0 and WW3, the root mean

137   square errors (RMSEs) of SST, significant wave height (SWH) and 10-m wind speed (WSP10) with

138   different coupling steps for the fully coupled experiment (ALL; details in Section 2.6) are calculated and

139   compared (Table S1 of the supplementary material). The three components are coupled every time step

140   (180 s) in 1_STEP_ALL experiment, every 5 steps (900 s) in 5_STEP_ALL experiment and every 10

141   steps (1800 s) in 10_STEP_ALL experiment. In 10_STEP_WW3, only the WW3 is coupled every 10

142   time steps, whereas the GFS and the MOM4 remain the one time step (180 s) coupling frequency as the

143   original settings in CFSv2.0. From Table S1, the 10_STEP_WW3 experiment has a relatively short

144   runtime and small RMSEs. Therefore, the time steps of the 10_STEP_WW3 are selected to compromise

145   computing time consumption and model RMSEs.

146   **2.2 Initialization of WAVEWATCH III**

147   In WW3, input of momentum and energy by wind, and dissipation for wave-ocean interaction are two

148   important terms (combined as input-dissipation source term) in the energy balance equation

149   (WAVEWATCH III Development Group, 2016), which include the estimation of the Charnock

150   parameter. Several different packages to calculate the input-dissipation source term (ST) are available in

151   the WW3 version 5.16, including ST2 (Tolman and Chalikov, 1996), ST3 (Janssen, 2004; Bidlot, 2012),

152   ST4 (Ardhuin et al., 2010), and ST6 (Zieger et al., 2015).

153   The initial wave fields were generated from 10-day simulation starting from rest in a stand-alone WW3

154   model. To minimize the biases of initial wave fields, we tested simulations with ST2, ST3, ST4, and ST6

155   schemes respectively, and compared the results with Janson-3 observations. Two 10-m wind datasets,

156   the Cross-Calibrated Multi-Platform (CCMP; Atlas et al., 2011) data and the fifth generation European

157   Centre for Medium-Range Weather Forecasts (ECMWF) Reanalysis (ERA5; Hersbach et al., 2020) data,

158   were used to drive the wave model respectively. Comparing all results, the ST4 scheme with ERA5 wind

159   forcing generates the minimum SWH bias (Table S2 in the supplementary material), consistent with

160   findings in Stopa et al. (2016). Thus, the ST4 scheme was chosen to calculate the input and dissipation

161   term, and generate initial wave fields with ERA5 wind forcing for experiments listed in Table 1. The

162   parameters used for ST4 scheme followed TEST471f from WAVEWATCH III Development Group

163   (2016), which is the CFSR (CFS Reanalysis) tuned setup and is commonly-used at global scale.

164   **2.3 Parameterizations of Stokes Drift-Related Ocean Mixing**

165   The full Stokes drift profile used in MOM4 is obtained by the method of Couvelard et al. (2020),

166   which is based on the work of Breivik et al. (2014; 2016). Breivik et al. (2016) derived the full Stokes

167   drift profile as

$$u_s B16(z) = u_s(0)[\exp(2k_p z) - \sqrt{-2\pi k_p z}\ \mathrm{erfc}(\sqrt{-2k_p z})], \qquad (1)$$

168   where $u_s(0)$ is the surface Stokes drift velocity, $k_p = \frac{u_s(0)}{6V_s}$, V_s is the Stokes transport, and erfc is

169   the complementary error function. Eqn. 1 is depth-averaged within each vertical grid interval as

$$u_s(z) = \frac{u_s(0)}{(th)_k}[I(z_{k+1/2}, k_p) - I(z_{k-1/2}, k_p)], \qquad (2)$$

$$I(z, k_p) = \frac{1}{6k_p}[e^{2k_p z} + 4k_p z \frac{u_s B16(z)}{u_s(0)}], \qquad (3)$$

170   where *th* is the thickness of layer *k*, following Li et al., (2017), Wu et al., (2019) and Couvelard et al.,

171   (2020).

172   **2.3.1 Mixing of Langmuir Turbulence**

173   McWilliams and Sullivan (2000) modified the turbulent velocity scale *W* in K-Profile Parameterization

174   (KPP) for vertical mixing by introducing an enhancement factor ε, to account for both boundary layer

175   depth changes and nonlocal mixing by Langmuir turbulence. Based on their work, Van Roekel et al.

176   (2012) improved the enhancement factor corresponding to alignment and misalignment of winds and

177   waves. Li et al. (2016) evaluated these parameterizations in a coupled global climate model, and found

178   that the difference between parameterizations with alignment and with misalignment was not significant,

179   owing to the relatively coarse resolution which cannot accurately represent the refraction by coasts and

180   current features. We used the parameterization from Van Roekel et al. (2012) as well. Because the

181   resolution in our model is relatively coarse too, and the angles between winds and waves are less than

182 30° in most areas (Fig. S1i&j in the supplementary material), we didn't consider misalignment in the

183 study.

184 W ($W=ku_*/\phi$, where u_* is the surface friction velocity, ϕ is the dimensionless flux profile, and

185 k=0.4 is the von Kármán constant) depends on the turbulent Langmuir number, that is,

$$W = \frac{ku_*}{\phi}\varepsilon, \tag{4}$$

$$\varepsilon = \sqrt{1 + (3.1La_\mathrm{t})^{-2} + (5.4La_\mathrm{t})^{-4}}, \tag{5}$$

186 where La_t is the turbulent Langmuir number, defined as

$$La_\mathrm{t} = \sqrt{\frac{u_*}{|u_s(0)|}}, \tag{6}$$

187 with $u_s(0)$ the surface Stokes drift velocity.

188 Furthermore, the enhanced W will influence the calculation of boundary layer depth. In KPP the

189 boundary layer depth is determined as the smallest depth at which the bulk Richardson number equals

190 the critical value $Ri_\mathrm{cr} = 0.3$, that is,

$$Ri_b(h) = \frac{gh[\rho_r - \rho(h)]}{\rho_0[|u_r - u(h)|^2 + W^2]} = Ri_\mathrm{cr}, \tag{7}$$

191 where g is acceleration of gravity, ρ is density, u is velocity, ρ_r is surface density, u_r is surface

192 velocity, ρ_0 is the average value of the density and h is the boundary layer depth. Hence, when W is

193 enhanced, the boundary layer depth h is deepened accordingly.

194 **2.3.2 Stokes-Coriolis Force and Associated Entrainment**

195 Because the Stokes drift velocity is an increment superimposed on the original current velocity, the

196 Coriolis force and the Stoke drift together produce an additional so-called Stokes-Coriolis (SC) force

197 (Hasselmann 1970), that is,

$$SC \; Force = \overrightarrow{u_s(z)} \times f\vec{z}. \qquad\qquad (8)$$

198 Here $\overrightarrow{u_s(z)}$ is the Stokes drift velocity vector, f is the Coriolis frequency, and $\vec{z}$ is the vertical unity

199 vector. For consistency, the Stokes drift velocity is also included in advection terms of tracers (e.g.,

200 temperature, salinity) and convergence terms (Law-Chune and Aouf, 2018; Couvelard et al., 2020). And

201 the free surface condition for barotropic mode is correspondingly modified to

$$\frac{\partial \eta}{\partial t} = -\nabla M_{curr} - \nabla M_{st}, \qquad\qquad (9)$$

202 where η is surface elevation, M_{curr} and M_{st} are the total vertical integral of regular Eulerian current

203 and Stokes drift, respectively.

204 To depict the entrainment below the ocean surface boundary layer induced by Stokes drift, Li et al.

205 (2016) suggested adding the square of surface Stokes drift velocity $(|u_s(0)|^2)$ to the denominator of

206 Eqn. 7, that is,

$$Ri_b(h) = \frac{gh[\rho_r - \rho(h)]}{\rho_0[|u_r - u(h)|^2 + W^2 + |u_s(0)|^2]} = Ri_{cr}. \qquad\qquad (10)$$

207 The boundary layer depth h in KPP from Eqn. 10 is then enhanced due to Stokes drift velocity.

208 **2.4 Stokes Drift and Sea Surface Current on Air-Sea Fluxes**

209 At the air-sea boundary layer, the momentum flux (τ), sensible heat flux (SH) and freshwater flux (E)

210 are calculated as

$$\tau = \rho_a C_d |\Delta \vec{V}| \Delta \vec{V}, \qquad\qquad (11)$$

$$SH = \rho_a C_h |\Delta \vec{V}| \Delta \theta, \qquad\qquad (12)$$

$$E = \rho_a C_e |\Delta \vec{V}| \Delta q, \qquad\qquad (13)$$

211 where C_d, C_h, C_e are surface exchange coefficients for momentum, sensible heat and freshwater. ρ_a

212 is air density. $\Delta\theta, \Delta q$ are potential temperature and humidity differences between air and sea, and $\Delta\vec{V}$

213 is velocity of air relative to water flow.

214   In CFSv2.0, $\Delta\vec{V}$ is set to be wind speed $(\overrightarrow{U_{wind}})$. However, the effect of ocean surface current should

215 not be ignored. Luo et al. (2005) first indicated that including ocean surface current $(\overrightarrow{U_{surf}})$ improves

216 estimates of τ and subsequent ocean response. Renault et al. (2016) further indicated that the

217 improvements of τ by $\overrightarrow{U_{surf}}$ also feed back into atmosphere. At present, $\Delta\vec{V} = \overrightarrow{U_{wind}} - \overrightarrow{U_{surf}}$ is

218 widely used in coupled ocean-atmosphere models (e.g., Hersbach and Bidlot, 2008; Takatama et al.,

219 2017; Renault et al., 2021). Furthermore, Bao et al. (2019) indicated that as a part of the sea surface water

220 movement with speed magnitude comparable to surface current in mid-high latitudes, the surface Stokes

221 drift $(\overrightarrow{u_s(0)})$ should also be included, that is,

$$\Delta\vec{V} = \overrightarrow{U_{wind}} - \overrightarrow{U_{surf}} - \overrightarrow{u_s(0)}. \qquad (14)$$

222 To account for the effects of the surface currents and of the Stokes drift, Eqn. 14 was used in the coupled

223 experiments (Table 1). To complete the coupling, the corresponding modification of the tridiagonal

224 matrix (Lemarié 2015) has been implemented in CFSv2.0. Note that the direction of Stokes drift is

225 generally consistent with 10-m wind (Fig. S1i&j in supplementary material), but the directions of surface

226 current and 10-m wind are usually different due to Coriolis effect (Fig. S1g&h). Consequently, the effects

227 of $\overrightarrow{U_{surf}}$ and $\overrightarrow{u_s(0)}$ on $\Delta\vec{V}$ depend on the angles between them and $\overrightarrow{U_{wind}}$.

228 **2.5 Parameterizations of Momentum Roughness**

229   In CFSv2.0, the fluxes of momentum, heat, and freshwater are passed from atmosphere to ocean, and

230 the estimates of them are critically important. The fluxes are in part determined by surface roughness

231 length, which can be converted to surface exchange coefficients based on the Monin-Obukhov similarity

232   theory (Monin and Obukhov, 1954).

233   **2.5.1 The Momentum Roughness Length in GFS**

234   In GFS, the momentum roughness length z_0 has two terms. The first term z_{ch} is parameterized by

235   the Charnock relationship (Charnock, 1955) representing wave-resulted sea surface roughness, and the

236   second term z_{vis} is the viscous contribution (Beljaars, 1994) for low winds and smooth surface, that is,

$$z_0 = z_{ch} + z_{vis} = \frac{C_{ch}u_*^2}{g} + \frac{0.11\nu}{u_*}. \tag{15}$$

237   Here $C_{ch} = 0.014$ is the constant Charnock parameter, ν is the air kinematic viscosity. The relation of

238   z_0 in GFS versus 10-m wind speed is shown in Fig.2 (black line).

239   **2.5.2 The Charnock Relationship Related to Wave State**

240   When ocean surface waves are explicitly considered, the Charnock parameter C_{ch} is not a constant

241   (Janssen 1989, 1991; Taylor and Yelland, 2001; Moon et al., 2004; Drennan et al., 2003, 2005). In the

242   study, we adopted a method developed by Moon et al. (2004), which considered the surface roughness

243   leveling off under extremely high wind speed (Powell et al., 2003; Donelan et al., 2004). Based on

244   observations, Moon et al. (2004) proposed Eqn. 16 to estimate the Charnock parameter by the wave age

245    $\frac{c_{pi}}{u_*}$ (c_{pi} is the peak phase speed of the dominant wind-forced waves) with constant values of a and b

246   changing with 10-m wind speed every 5 m/s in the range of 10 m/s to 50 m/s.

$$C_{ch} = a(\frac{c_{pi}}{u_*})^b, \tag{16}$$

247   To obtain continuous values of a and b, we derive a new relationship (Eqn. 17) to estimate a and b from

248   10-m wind speed U_{10} by fitting the values in Table 1 of Moon et al. (2004),

$$a = \frac{1}{0.1477U_{10}{}^2 - 0.7395U_{10} - 10.9995},$$

(17)

$$b = 1.5661E^{-5}U_{10}{}^3 - 0.002U_{10}{}^2 + 0.1017U_{10} - 1.6182.$$

249   Because the observations in Moon et al. (2004) were obtained under tropical cyclones, Eqn. 17 is used

250   for U_{10}>15 m/s, whereas the original Charnock relationship of WW3 ST4 scheme (Janssen 1989, 1991)

251   is used for U_{10} ≤15 m/s. The revised parameterization is called ST4-M04. Figure S2 in supplementary

252   material shows the C_{ch} distribution obtained by Eqn. 16-17. In general small wind direction variations

253   at low latitudes lead to large wave age and thus low C_{ch}. The situation is opposite at mid-high latitudes.

254   The relationships between z_0 and U_{10} in GFS, WW3 ST4 scheme (Janssen 1989, 1991) and ST4-

255   M04 scheme were compared in Fig.2. The z_0 in GFS increases relatively slowly with increasing wind

256   speed (black). The value of z_0 from ST4 scheme (purple) increases rapidly with wind speed at high

257   winds. In comparison, in ST4-M04 scheme (blue) the rapid increase of z_0 at high wind speed is

258   obviously restrained, although the mean z_0 is slightly higher than that in GFS at wind speed >10 m/s

259   due to larger C_{ch} (>0.014 in Fig. S2). Furthermore, since the Charnock number is constant in GFS, the

260   standard deviation (STD) of z_0 at a given wind speed is near zero. Since the z_0 is determined only by

261   wind-sea conditions in ST4 and ST4-M04 scheme, the STD at a given wind speed is mainly owing to

262   variations in wind fetch and development stage of sea state. The reduced STDs in ST4-M04 scheme,

263   compared to ST4, imply less sensitivity of z_0 to fetch and sea state. Note that the ST4-M04 is used in

264   GFS, while the z_0 in WW3 is still calculated by the ST4 source term to avoid affecting the balance of

265   adjusted wind input and dissipation.

266   **2.6 Set of Experiments**

267   A series of numerical experiments was conducted to evaluate the effects of aforementioned wave-

268   related processes on ocean and atmosphere in two 56-day periods, from January 3 to February 28, 2017

269   and from August 3 to September 28, 2018 for boreal winter and boreal summer, respectively.

270   The reference experiment (CTRL) is a one-way coupled experiment, in which CFSv2.0 provides 10-

271   m wind and surface current to WW3, whereas no variable is transferred from WW3 to CFSv2.0. The

272   results of CFSv2.0 in CTRL are consistent with the corresponding CFS Reanalysis data (Saha et al.,

273   2010). For each period, four sensitivity experiments were carried out (Table 1). Based on CTRL, the first

274   is the VR12-AL-SC-EN experiment, in which the Langmuir mixing parameterization is used with

275   Stokes-Coriolis force and entrainment in MOM4. The second is the Z0-M04 experiment, in which the

276   constant C_{ch} in GFS is replaced by C_{ch} from WW3 ST4-M04 scheme. The effect of fluxes in GFS

277   generated by $\Delta \vec{V}$ (Eqn. 14) is tested in the FLUX experiment. The last experiment is the ALL, which

278   includes all three parameterizations.

279   **3 Data**

280   Due to the availability of in situ and reanalysis data in the simulation periods, only sea surface

281   temperature (SST), ocean subsurface temperature and salinity (T/S), 2-m air temperature (T02), 10-m

282   wind speed (WSP10), and significant wave height (SWH) were used to evaluate the simulation results.

283   The daily average satellite Optimum Interpolation SST (OISST) data were obtained from NOAA, with

284   0.25°×0.25° resolution (Reynolds et al., 2007; https://www.ncdc.noaa.gov/oisst). The global Argo

285   observational profiles of T/S (Li et al., 2019) were from China Argo Real-time Data Center

286   (www.argo.org.cn). The ERA5 datasets of T02, WSP10 and SWH with a spatial resolution of 0.5° were

287   also used (Hersbach et al., 2020; https://cds.climate.copernicus.eu/cdsapp#!/dataset/reanalysis-era5-

288   single-levels), which assimilated huge amounts of historical data and thus provided reliable hourly

289   estimates. Additionally, the WSP10 and SWH observations from the available National Data Buoy

290   Center (NDBC) buoy data (https://www.ndbc.noaa.gov) were used for comparison.

291   **4 Experimental Results**

292   In this section, an evaluation of simulation results was presented. Comparisons were made between

293   model results and observations/reanalysis data. The results in the first three days were excluded in the

294   evaluation, since the wave influences were weak at the beginning. Compared with observations or ERA5,

295   the general increase of the biases in all experiments is likely a drift from the initial conditions since no

296   data are assimilated.

297   **4.1 Sea Surface Temperature (SST) and 2-m Air Temperature (T02)**

298   Figure 3a shows the spatial distribution of 53-day (day 4 to day 56) averaged SST biases in CTRL in

299   boreal winter, defined as SST in CTRL minus OISST. The global mean SST bias is approximately $0.32℃$,

300   and the average RMSE is about $1.09℃$ from day 4 to day 56 in CTRL (Fig. 3a). The simulated SSTs are

301   generally overestimated, and the large biases ($>1.0℃$) are mainly distributed in the Southern Ocean. In

302   Fig. 3b, the global-averaged RMSEs of CTRL (black) increase with time in the first month and then

303   gradually level off. Compared with CTRL, the RMSEs are reduced continuously in VR12-AL-SC-EN

304   and ALL (yellow and red), but not in Z0-M04 and FLUX (purple and blue).

305   To understand the critical process responsible for the bias reduction in ALL, the SST differences are

306   compared across all four experiments (Fig.3c-f). Clearly, the difference in experiment VR12-AL-SC-EN

307   is similar to that in ALL (Fig. 3c&3f). The spatial correlation coefficient between the SST differences

308   with CTRL of the two experiments (Fig. 3c&3f) is 0.67, significant at 99% confidence level, and the

309　RMSEs of SST are not different significantly (red and yellow lines in Fig. 3b), indicating the Stokes

310　drift-related parameterizations in VR12-AL-SC-EN mainly contribute to the SST positive bias reduction.

311　This contrasts with Couvelard et al. (2020), where SST overestimations and MLD underestimations are

312　reduced mainly due to the directly modified turbulence kinetic energy scheme. The global mean SST

313　bias in ALL is 0.02 ℃ with RMSE of 1.03℃, and in most areas the SST differences compared with

314　CTRL are significant (P ≤0.05) (dotted areas in Fig. 3f). Large SST improvements mainly appear in the

315　Southern Ocean, with a regional RMSE decrease from 1.27 to 1.04 ℃ south of 45°S (Fig. 3f and red

316　line in Fig. 5a). The reduction of overestimated SSTs in CTRL (red in Fig 3a) is because the Stokes drift-

317　related parameterizations in MOM4 inject turbulent kinetic energy into the ocean, which enhance vertical

318　mixing, and subsequently cool the surface waters (Belcher et al., 2012; Li et al. 2016). The modified

319　roughness and relative velocity in Z0-M04 and FLUX also influence upper ocean mixing (Fig. 3d&e)

320　via changing momentum flux, and lead to generally warmer SSTs (purple and blue lines in Fig. 3b&5a).

321　The effect from Stokes drift-related ocean mixing parameterizations dominates SST changes in ALL.

322　　In boreal summer, the global mean SST bias in CTRL is overestimated approximately 0.29℃, and the

323　averaged RMSE from day 4 to day 56 is about 1.19℃. The overestimated SSTs (>1.0℃) mainly occur

324　in the Northern Hemisphere (Fig. 4a). The global-averaged RMSEs are also generally lower in VR12-

325　AL-SC-EN and ALL than in CTRL (Fig. 4b). The cooling effects in VR12-AL-SC-EN lead to a global

326　mean bias of 0.06℃, and the large SST improvements mainly occur north of 50°N (Fig. 4c and yellow

327　line in Fig. 5b). The changes of SST in Z0-M04 and FLUX (Fig. 4d&e; purple and blue lines in Fig.

328　4b&5b) are relatively small. The global mean bias in ALL is 0.04℃ with an RMSE of 1.14℃ (Fig. 4f).

329　　As aforementioned, large improvements of overestimated SST mainly occur at mid-high latitudes in

330　local summer. The time series of RMSEs and correlation coefficients of SST between model and

17

331   observation in the region (0-360°E, 45°-78°S in boreal winter and 0-360°E, 50°-78°N in boreal summer)

332   are shown in Fig. 5c-f. The RMSEs in CTRL (blue in Fig. 5c&d) increase in the first few weeks and then

333   gradually decrease afterward. Compared with CTRL, RMSEs in VR12-AL-SC-EN (yellow) and ALL

334   (red) are significantly (P ≤0.01) reduced by about 0.3℃. The spatial correlation coefficients decrease

335   with time but remain high (>0.90) for all experiments (Fig. 5e&f) with higher values in experiment

336   VR12-AL-SC-EN (yellow).

337   We also compared T02 from experiments with ERA5 (Fig. 6). Warm biases of T02 appear in both

338   winter and summer in CTRL (Fig. 6a&b). The changes of T02 in sensitivity experiments (Fig. 6c-j) are

339   generally consistent with the changes of SST in the same experiments (Fig.3&4). The correlation

340   coefficients between the SST and the T02 changes for the ALL experiment in boreal winter and summer

341   (Fig. 3f&6f and Fig. 4f&6j) are 0.61 and 0.53 respectively, significant at 99% confidence level. In boreal

342   winter, all wave-coupled experiments except FLUX reduce the T02 mean bias (Fig.6c-f). VR12-AL-SC-

343   EC has the largest T02 bias reduction compared with CTRL, from 0.55℃ to 0.17℃ (Fig.6c). In boreal

344   summer, both VR12-AL-SC-EC and ALL have the largest T02 bias reduction, from 0.29℃ to 0.08℃

345   (Fig.6g&j). Noticeably, the improvements in RMSEs are not large for all experiments, because the

346   improvements mainly occur in areas with overestimated temperature.

347   **4.2 Mixed Layer Depth (MLD)**

348   To further evaluate the direct effect of the wave-related processes on the upper ocean, we compared

349   the MLD of all experiments with that estimated from Argo profiles in summer. The simulated T/S were

350   interpolated onto the positions of Argo profiles at the nearest time. The MLD was estimated as the depth

351   where the change of potential density reaches the value corresponding to a 0.2℃ decrease of potential

352   temperature with unchanged salinity from surface (de Boyer Montégut et al., 2004; Wang and Xu, 2018).

353   The time series of MLDs from numerical experiments and Argo south of 45°S in boreal winter (north

354   of 45°N in boreal summer) are compared in Fig. 7a (7b). The simulated MLDs are generally within the

355   STD of Argo MLDs (shading in Fig. 7). In CTRL, the mean bias (CTRL minus Argo) with STD is -

356   13.15±7.82 m (-6.75±5.29 m) in boreal winter (summer). The correlation coefficient of MLDs in CTRL

357   with Argo MLDs is 0.55 (0.68) with P ≤0.01, and the mean RMSE is 15.30 m (8.55 m) in boreal winter

358   (summer). In ALL, the mean bias (ALL minus Argo) with STD is 7.70±10.42 m (3.30±7.78 m) in boreal

359   winter (summer), and the correlation coefficient of MLDs enhances to 0.63 (0.78). The RMSE south of

360   45°S decreases from 15.30 m in CTRL to 12.96 m in ALL. The RMSE north of 45°N decreases from

361   6.71 m in CTRL to 5.55 m in ALL in the first six weeks but the value increases in the last two weeks due

362   to overestimation of MLDs. Compared with CTRL (orange in Fig. 7), VR12-AL-SC-EN (yellow) and

363   ALL (dark blue) show significant improvements (P ≤0.01) on the underestimated MLDs time series,

364   whereas the MLDs difference between CTRL and Z0-M04 (purple)/FLUX (blue) is non-significant.

365   **4.3 Wind Speed at 10 m (WSP10) and Significant Wave Height (SWH)**

366   Compared with ERA5, the WSP10s in CTRL are generally overestimated in both winter and summer

367   (Fig.8a&9a). The global averaged RMSEs of WSP10s in CTRL are 4.25 m/s (4.26 m/s) in boreal winter

368   (summer). The global averaged RMSEs of WSP10s in all experiments increase with time in the first two

369   weeks and then gradually level off (Fig. 8b&9b). The differences of RMSEs between CTRL and other

370   experiments are tiny in the first 10 days, and afterwards the RMSEs in Z0-M04 and ALL (purple and

371   red) become clearly smaller than in CTRL over most of the time.

372   The comparisons of the simulated SWHs in CTRL with the ERA5 also show that the SWHs are

373   overestimated in both winter and summer (Fig. 10a&11a). In boreal winter, the global mean SWH bias

374   in CTRL is approximately 0.20 m with overestimates (> 0.30 m) in the Pacific, the North Atlantic and

375   the Southern Ocean (Fig.10a), and the average RMSE is about 1.29 m. In boreal summer, the global

376   mean bias in CTRL is approximately 0.17 m with 1.22 m RMSE (Fig. 11a). Similar to WSP10s, the

377   RMSEs of SWHs also increase in the first two weeks and then gradually level off (Fig. 10b&11b). The

378   RMSEs in Z0-M04 and ALL (purple and red) are smaller than in CTRL over most of the time, consistent

379   with changes of WSP10s. The correlation coefficients between changes of WSP10s and changes of

380   SWHs in ALL are 0.77 and 0.73 in boreal winter and summer respectively (Fig. 8f&10f and Fig. 9f&11f),

381   significant at 99% confidence level, indicating that the SWHs changes are closely related to changes of

382   wind speeds.

383   In VR12-AL-SC-EN, the reduction of SST warm biases affects air temperature and stabilizes the

384   marine atmospheric boundary layer (Sweet et al. 1981; O'Neill et al. 2003), and subsequently reduces

385   WSP10s and SWHs with decreased global bias in boreal winter (Fig.8c&10c). In Z0-M04, the

386   overestimated WSP10s and SWHs are also reduced (Fig. 8d&10d) due to the larger z_0 with the ST4-

387   M04 scheme at wind speed > 10 m/s (Fig. 2). The increase of z_0 enhances wind stress and momentum

388   transferred into the ocean, and therefore reduces surface winds (Pineau-Guillou et al. 2018; Sauvage et

389   al. 2020) and consequently reduces SWHs. In FLUX (Fig. 8e&10e), $\overrightarrow{U_{surf}}$ and $\overrightarrow{u_s(0)}$ decrease wind

390   stress and momentum transfer when their directions are consistent with wind directions, and vice versa

391   (Hersbach and Bidlot, 2008; Renault et al., 2016). For instance, the angles between wind and current are

392   relatively small (<90°) in the northeastern Pacific, reducing the wind stress and thus enhancing WSP10s

393   (Fig. 8e). In contrast, the large angles (>90°) between the northwesterlies and the Kuroshio in the

394   northwestern Pacific enhance wind stress, and decrease WSP10s (Fig. 8e). Consequently, improvements

395   occur in areas with misalignment of winds and currents. With all combined effects, the biases of WSP10s

396   and SWHs in ALL in most regions are decreased (Fig. 8f&10f), with the reduced global RMSEs of 4.17

397   m/s and 1.18 m respectively. In boreal summer, the improvements of WSP10s and SWHs are relatively

398   small in terms of global averaged RMSEs, because of smaller positive biases in CTRL (Fig. 9a&11a). In

399   ALL, the global averaged bias of WSP10s (SWHs) is -0.01 m/s (0.03 m). The largest reduction primarily

400   appears in the Southern Ocean (Fig. 9f&11f) to improve the overestimated westerlies and SWHs in CTRL

401   (Fig. 9a&11a).

402   Previous studies indicated that ocean surface winds in ERA5 are underestimated in some regions

403   (Belmonte Rivas and Stoffelen 2019; Kalverla et al. 2020; Sharmar and Markina 2020). To better

404   demonstrate the effects of waves on WSP10s and SWHs, comparisons of WSP10s and SWHs with the

405   NDBC buoy data are made (Table 2 and Fig. 12). The differences between sensitivity experiments and

406   CTRL are all statistically significant at 95% confidence level. Buoys are mainly located in the

407   northeastern Pacific, the tropical Pacific and the northwestern Atlantic oceans (Fig. S3), and buoy

408   identifiers with total numbers, longitudes and latitudes are listed in Table S3. The method from Hsu et al.

409   (1994) was used to adjust wind speeds from buoy data to the reference height of 10 m.

410   Compared to the NDBC data, the WSP10s and the SWHs in CTRL are generally overestimated in both

411   winter and summer with positive mean biases (Table 2 and Fig. 12). The reduction of mean biases appears

412   in all experiments except FLUX in boreal winter. The wave-related processes are most effective in areas

413   with positive biases, consistent with previous comparisons with ERA5. In boreal winter, the angles

414   between winds and currents are small. The wind stresses are then reduced in FLUX, and the WSP10s are

415   enhanced. So the positive bias is further enhanced. The improvements in ALL are generally the largest

416   (Table 2), with the WSP10s RMSE of 1.04 m/s (1.15 m/s) and the SWHs RMSE of 0.36 m (0.24 m) in

21

417   boreal winter (summer). As shown in Fig. 12, with the increase of WSP10s and SWHs, the reduction of

418   overestimation in ALL compared with CTRL is more prominent.

419   **5 Summary and Discussion**

420   To investigate the individual role played by wave-related processes on atmosphere and ocean interface

421   in a coupled global atmosphere-ocean-wave modelling system on intraseasonal scale, we implemented

422   the version 5.16 of WW3 into CFSv2.0 for global oceans from 78ºS-78ºN, using the C-Coupler2. In this

423   coupled system, the WW3 was forced by 10-m wind and surface current generated in CFSv2.0. Stokes

424   drift-related Langmuir mixing, Stokes-Coriolis force and entrainment in ocean, air-sea fluxes modified

425   by surface current and Stokes drift, and momentum roughness length (z_0) were considered separately,

426   and the results of sensitivity experiments were compared against in-situ buoys, satellite measurements

427   and ERA5 reanalysis. The effects of waves on intraseasonal prediction were examined in two 56-day

428   cases, one for boreal winter and the other one for boreal summer.

429   The following key results were found:

430   1. Overestimated SST, T02 and underestimated MLD in the mid-high latitudes in CFSv2.0 are

431   significantly improved, particularly in local summer. Because enhanced vertical mixing

432   generated by Langmuir turbulence, Stokes-Coriolis force and entrainment in VR12-AL-SC-

433   EN changes temperature structure in the upper ocean, and further affects air temperature. In

434   boreal winter, the regional RMSE of SST (T02) in the Southern Ocean decreases from 1.27

435   (1.93) in CTRL experiment to 1.04 (1.67) ℃ in ALL experiment. In boreal summer, the effect

436   is weaker because of the smaller ocean areas in the mid-high latitudes of the Northern

437   Hemisphere.

438   2. In general, all wave-related processes reduce biases for WSP10s and SWHs, particularly in

439   regions where WSP10s and SWHs are overestimated. The decreased SSTs in VR12-AL-SC-

440   EN stabilize the marine atmospheric boundary layer, and lead to weakened WSP10s and SWHs.

441   The modified roughness in Z0-M04 generally enhances momentum transfer into the ocean, and

442   so decreases WSP10s and SWHs. The relative wind-wave-current speed in FLUX also affects

443   wind stress, and further influences WSP10s and SWHs. Compared with NDBC buoy

444   observations and ERA5, the ALL experiment shows significant improvements.

445   In addition to the variables aforementioned, the changes of simulated enthalpy fluxes were also

446   compared, which mainly depend on the WSP10s changes. However, the wave-related effects on enthalpy

447   fluxes are non-significant for the 2-month simulation, so the results are not shown.

448   The wave-related parameterizations used in the study mainly improve model biases at mid-high

449   latitudes, and SST biases in tropical oceans are only slightly improved (Fig. 3&4). Breivik et al. (2015)

450   improved SST as well as subsurface temperature simulations in Nucleus for European Modelling of the

451   Ocean (NEMO) with parametrizations including the wave-related Charnock parameter, modification of

452   water-side stress with wind input and wave dissipation, wave dissipation-related turbulent kinetic energy

453   flux and the Stokes-Coriolis force. Based on a global NEMO-WW3 coupled framework, Couvelard et al.

454   (2020) modified the Charnock parameter, the Stokes drift-related forces and the Langmuir cell with

455   misalignment of winds and waves, the oceanic surface momentum flux and the turbulence kinetic energy

456   to reduce SST and MLD biases. In addition, sea sprays can enhance air-sea heat fluxes in the tropics

457   (Andreas et al. 2008; Andreas et al. 2015). We will consider more processes in future studies.

458   Different parameterizations for the same wave-related process also deserve discussion. For ocean

459   surface roughness, the most classic parametrizations are those developed by Janssen (1989, 1991), Taylor

460 and Yelland (2001) and Drennan et al. (2003). The method of Taylor and Yelland (2001) requires the

461 peak wavelength for the total spectrum, whereas that of Drennan et al. (2003) only requires the peak of

462 wind-sea waves. This difference leads to the fact that the former is more suitable for a mixed sea state,

463 while the latter is more suitable for a young sea state (Drennan et al., 2005). And the effect of Janssen's

464 parameterization (1989, 1991) is similar to that of Drennan et al. (2003), since it is also based on the

465 wind-sea conditions (Shimura et al., 2017).

466 The case studies indicate that there remain significant biases in the coupled system, probably owing

467 to inaccuracy of coarse resolution, absence of a coupled wave-ice modular, and deficiency of initial fields.

468 In addition, to further improve the model and eliminate the biases, as Breivik et al. (2015) proposed,

469 extra adjusting of the individual model components in the coupled systems is also necessary. All of these

470 require further efforts to investigate efficient methods to improve fully coupled systems.

471 **Code and data availability**

472 The code developed for the coupled system can be found under https://doi.org/10.5281/zenodo.5811002

473 (Shi et al., 2021), including the coupling, preprocessing, run control and postprocessing scripts. The

474 initial fields for CFSv2.0 are generated by the real time operational Climate Data Assimilation System,

475 downloaded   from   the   CFSv2.0   official   website

476 (http://nomads.ncep.noaa.gov/pub/data/nccf/com/cfs/prod). The daily average satellite Optimum

477 Interpolation SST (OISST) data are obtained from NOAA (https://www.ncdc.noaa.gov/oisst), and the

478 National Data Buoy Center (NDBC) buoy data are also obtained from NOAA

479 (https://www.ndbc.noaa.gov). The Argo observational profiles of T/S are available at China Argo Real-

480 time Data Center (www.argo.org.cn). The ERA5 reanalysis are available at the Copernicus Climate

481 Change Service (C3S) Climate Date Store

482 (https://cds.climate.copernicus.eu/cdsapp#!/dataset/reanalysis-era5-single-levels).

483 **Author contribution**

484 FX and RS designed the experiments and RS carried them out. RS developed the code of coupling

485 parametrizations and produced the figures. ZF contributed to the installation and operation of CFSv2.0.

486 LL and HY contributed to the application of C-Coupler2. XL and YZ provided the original code of

487 CFSv2.0. RS prepared the manuscript with contributions from all co-authors. FX and HL contributed to

488 review and editing.

496 **References**

497 Andreas, E. L., Mahrt, L., and Vickers, D.: An improved bulk air-sea surface flux algorithm, including

498 spray-mediated transfer, Quarterly Journal of the Royal Meteorological Society, 141, 642-654, 2015.

499 Andreas, E. L., Persson, P. O. G., and Hare, J. E.: A bulk turbulent air-sea flux algorithm for high-wind,

500 spray conditions, Journal of Physical Oceanography, 38, 1581-1596, 2008.

501   Ardhuin, F., Rogers, E., Babanin, A. V., Filipot, J., Magne, R., Roland, A., Der Westhuysen, A. V.,

502   Queffeulou, P., Lefevre, J. M., and Aouf, L.: Semiempirical Dissipation Source Functions for Ocean

503   Waves. Part I: Definition, Calibration, and Validation, Journal of Physical Oceanography, 40, 1917-1941,

504   http://dx.doi.org/10.1175/2010JPO4324.1, 2010.

505   Atlas, R., Hoffman, R. N., Ardizzone, J., Leidner, S. M., Jusem, J. C., Smith, D. K., and Gombos, D.: A

506   Cross-calibrated, Multiplatform Ocean Surface Wind Velocity Product for Meteorological and

507   Oceanographic Applications, Bulletin of the American Meteorological Society, 92, 157-174,

508   http://dx.doi.org/10.1175/2010BAMS2946.1, 2011.

509   Bao, Y., Song, Z., & Qiao, F.: FIO-ESM version 2.0: Model description and evaluation. Journal of

510   Geophysical Research: Oceans, 125, e2019JC016036. https://doi.org/10.1029/2019JC016036, 2019.

511   Belcher, S. E., Grant, A. L. M., Hanley, K., Foxkemper, B., Van Roekel, L., Sullivan, P. P., Large, W. G.,

512   Brown, A. R., Hines, A., and Calvert, D.: A global perspective on Langmuir turbulence in the ocean

513   surface boundary layer, Geophysical Research Letters, 39, http://dx.doi.org/10.1029/2012GL052932,

514   2012.

515   Beljaars, A. C. M.: The parametrization of surface fluxes in large-scale models under free convection. Q.

516   J. R. Meteorol. Soc., 121, 255{270. https://doi.org/10.1002/qj.49712152203, 1994.

517   Belmonte Rivas, M., and Stoffelen, A.: Characterizing ERA-Interim and ERA5 surface wind biases using

518   ASCAT, Ocean Science, 15, 831-852, 10.5194/os-15-831-2019, 2019.

519   Bidlot, J.-R., Prates, F., Ribas, R., et al.: Enhancing tropical cyclone wind forecasts, ECMWF newsletter,

520   164, 33-37. https://www.ecmwf.int/en/newsletter/164/meteorology/enhancing-tropical-cyclonewind-

521   forecasts, 2020.

522 Bidlot, J.-R.: Model upgrade improves ocean wave forecasts. ECMWF newsletter, 159, 10-10.

523 https://www.ecmwf.int/en/newsletter/159/news/modelupgrade-improves-ocean-wave-forecasts, 2019.

524 Bidlot, J.-R.: Present status of wave forecasting at ECMWF, Workshop on ocean waves, 25-27, 2012.

525 Breivik, Ø., Bidlot, J.-R., and Janssen, P. A.: A Stokes drift approximation based on the Phillips spectrum,

526 Ocean Modelling, 100, 49-56, 2016.

527 Breivik, Ø., Janssen, P. A., and Bidlot, J.-R.: Approximate Stokes drift profiles in deep water, Journal of

528 Physical Oceanography, 44, 2433-2445, 2014.

529 Breivik, Ø., Mogensen, K., Bidlot, J., Balmaseda, M., and Janssen, P. A. E. M.: Surface wave effects in

530 the NEMO ocean model: Forced and coupled experiments, Journal of Geophysical Research, 120, 2973-

531 2992, http://dx.doi.org/10.1002/2014JC010565, 2015.

532 Charnock, H.: Wind stress on a water surface, Quarterly Journal of the Royal Meteorological Society, 81,

533 639-640, http://dx.doi.org/10.1002/qj.49708135027, 1955.

534 Couvelard, X., Lemarié, F., Samson, G., Redelsperger, J.-L., Ardhuin, F., Benshila, R., and Madec, G.:

535 Development of a two-way-coupled ocean-wave model: assessment on a global NEMO(v3.6)-

536 WW3(v6.02) coupled configuration, Geosci. Model Dev., 13, 3067-3090, https://doi.org/10.5194/gmd-

537 13-3067-2020, 2020.

538 de Boyer Montégut, C., Madec, G., Fischer, A. S., Lazar, A., and Iudicone, D.: Mixed layer depth over

539 the global ocean: An examination of profile data and a profile‐based climatology, Journal of

540 Geophysical Research, 109, http://dx.doi.org/10.1029/2004JC002378, 2004.

541 Donelan, M. A., Haus, B. K., Reul, N., Plant, W. J., Stiassnie, M., Graber, H. C., Brown, O. B., and

542 Saltzman, E. S.: On the limiting aerodynamic roughness of the ocean in very strong winds, Geophysical

543 Research Letters, 31, 10.1029/2004gl019460, 2004.

544   Drennan, W. M., H. C. Graber, D. Hauser, and C. Quentin: On the wave age dependence of wind stress

545   over pure wind seas, J. Geophys. Res., 108(C3), 8062, doi:10.1029/2000JC000715, 2003.

546   Drennan, W. M., P. K. Taylor, and M. J. Yelland: Parameterizing the sea surface roughness, J. Phys.

547   Oceanogr., 35(5), 835-848, 2005.

548   ECMWF: Official IFS Documentation CY47R1. In chap. PART VII: ECMWF wave model. Reading,

549   UK: ECMWF, 10.21957/31drbygag, 2020.

550   Fan, Y., Lin, S., Held, I. M., Yu, Z., and Tolman, H. L.: Global Ocean Surface Wave Simulation Using a

551   Coupled Atmosphere-Wave Model, Journal of Climate, 25, 6233-6252, http://dx.doi.org/10.1175/JCLI-

552   D-11-00621.1, 2012.

553   Ghantous, M., and Babanin, A. V.: One-dimensional modelling of upper ocean mixing by turbulence due

554   to wave orbital motion, Nonlinear Processes in Geophysics, 21, 325-338, 10.5194/npg-21-325-2014,

555   2014.

556   Griffies, S. M., Harrison, M. J., Pacanowski, R. C., and Rosati, A.: A technical guide to MOM4, GFDL

557   Ocean Group Tech. Rep, 5, 342, 2004.

558   Hasselmann, K.: Wave-driven inertial oscillations, Geophysical and Astrophysical Fluid Dynamics, 1,

559   463-502, http://dx.doi.org/10.1080/03091927009365783, 1970.

560   Hersbach H. and Bidlot, J.-R.: The relevance of ocean surface current in the ECMWF analysis and

561   forecast system. Proceeding from the ECMWF Workshop on Atmosphere-Ocean Interaction, 10-12,

562   https://www.ecmwf.int/sites/default/files/elibrary/2009/9866-relevance-ocean-surface-current-ecmwf-

563   analysis-and-forecast-system.pdf, 2008.

564   Hersbach, H., Bell, B., Berrisford, P., Hirahara, S., et al.: The ERA5 Global Reanalysis, Quarterly Journal

565   of the Royal Meteorological Society, Soc. 00: 363 (2020), https://doi.org/10.1002/qj.3803, 2020.

566   Hsu, S. A., Eric A. Meindl, and David B. Gilhousen: Determining the Power-Law Wind-Profile Exponent

567   under Near-Neutral Stability Conditions at Sea, Applied Meteorology, Vol. 33, No. 6,

568   https://doi.org/10.1175/1520-0450(1994)033<0757:DTPLWP>2.0.CO;2, 1994.

569   Janssen, P. A. E. M.: The interaction of ocean waves and wind, Cambridge University Press, pp 312,

570   2004.

571   Janssen, P. A. E. M.: The Quasi-linear theory of wind wave generation applied to wave forecasting. J.

572   Phys.   Oceanogr.   21,   1631-1642.   https://doi.org/10.1175/1520-

573   0485(1991)021<1631:QLTOWW>2.0.CO;2, 1991.

574   Janssen, P. A. E. M.: Wave-induced stress and the drag of air flow over sea waves. J. Phys. Oceanogr.

575   19(6), 745-754. https://doi.org/10.1175/1520-1310 0485(1989)019<0745:WISATD>2.0.CO;2, 1989.

576   Kalnay, E., Kanamitsu, M., Kistler, R., Collins, W. D., Deaven, D. G., Gandin, L. S., Iredell, M. D., Saha,

577   S., White, G. H., and Woollen, J.: The NCEP/NCAR 40-Year Reanalysis Project, Bulletin of the

578   American   Meteorological   Society,   77,   437-471,   http://dx.doi.org/10.1175/1520-

579   0477(1996)077%3C0437:TNYRP%3E2.0.CO;2, 1996.

580   Kalverla, P. C., Holtslag, A. A. M., Ronda, R. J., and Steeneveld, G.-J.: Quality of wind characteristics

581   in recent wind atlases over the North Sea, Quarterly Journal of the Royal Meteorological Society, 146,

582   1498-1515, 10.1002/qj.3748, 2020.

583   Kukulka, T., Plueddemann, A. J., Trowbridge, J. H., and Sullivan, P. P.: Significance of Langmuir

584   circulation in upper ocean mixing: comparison of observations and simulations, Geophysical Research

585   Letters, 36, http://dx.doi.org/10.1029/2009GL037620, 2009.

586   Law-Chune, S., and Aouf, L.: Wave effects in global ocean modeling: parametrizations vs. forcing from

587   a wave model, Ocean Dynamics, 68, 1739-1758, http://dx.doi.org/10.1007/s10236-018-1220-2, 2018.

588   Lemarié, F.: Numerical modification of atmospheric models to include the feedback of oceanic currents

589   on air-sea fluxes in ocean-atmosphere coupled models, INRIA Grenoble-Rhône-Alpes, Laboratoire Jean

590   Kuntzmann, https://hal.inria.fr/hal-01184711/document, 2015.

591   Li, D., Staneva, J., Bidlot, J.-R., Grayek, S., Zhu, Y., and Yin, B.: Improving Regional Model Skills

592   During Typhoon Events: A Case Study for Super Typhoon Lingling Over the Northwest Pacific Ocean,

593   Frontiers in Marine Science, 8, 10.3389/fmars.2021.613913, 2021.

594   Li, M., and Garrett, C.: Mixed Layer Deepening Due to Langmuir Circulation, Journal of Physical

595   Oceanography,   27,   121-132,   http://dx.doi.org/10.1175/1520-

596   0485(1997)027%3C0121:MLDDTL%3E2.0.CO;2, 1997.

597   Li, Q., Foxkemper, B., Breivik, O., and Webb, A.: Statistical models of global Langmuir mixing, Ocean

598   Modelling, 113, 95-114, http://dx.doi.org/10.1016/j.ocemod.2017.03.016, 2017.

599   Li, Q., Webb, A., Foxkemper, B., Craig, A., Danabasoglu, G., Large, W. G., and Vertenstein, M.:

600   Langmuir mixing effects on global climate: WAVEWATCH III in CESM, Ocean Modelling, 103, 145-

601   160, http://dx.doi.org/10.1016/j.ocemod.2015.07.020, 2016.

602   Li, Z., Liu, Z., & Xing, X.: User Manual for Global Argo Observational data set (V3.0) (1997-2019),

603   China Argo Real-time Data Center, Hangzhou, 37pp, 2019.

604   Liu, L., Zhang, C., Li, R., and Wang, B.: C-Coupler2: a flexible and user-friendly community coupler for

605   model   coupling   and   nesting,   Geoscientific   Model   Development   Discussions,   11,   1-63,

606   http://dx.doi.org/10.5194/gmd-11-3557-2018, 2018.

607   Luo, J.J., Masson, S., Roeckner, E., Madec, G., & Yamagata, T.: Reducing climatology Bias in an ocean-

608   atmosphere   CGCM   with   improved   coupling   physics.   Journal   of   Climate,   18(13),   2344-2360.

609   https://doi.org/10.1175/JCLI3404.1, 2005.

610   Mcwilliams, J. C., and Sullivan, P. P.: Vertical Mixing by Langmuir Circulations, Spill Science &

611   Technology Bulletin, 6, 225-237, http://dx.doi.org/10.1016/S1353-2561(01)00041-X, 2000.

612   Monin, A. S., and Obukhov, A. M.: Basic laws of turbulent mixing in the surface layer of the atmosphere,

613   Contrib. Geophys. Inst. Acad. Sci. USSR, 151(163), e187, 1954.

614   Moon, I., Ginis, I., and Hara, T.: Effect of surface waves on Charnock coefficient under tropical cyclones,

615   Geophysical Research Letters, 31, http://dx.doi.org/10.1029/2004GL020988, 2004.

616   Moum J.N., and Smyth W.D.: Upper Ocean Mixing. In Cochran, J. Kirk; Bokuniewicz, J. Henry; Yager,

617   L. Patricia (Eds.) Encyclopedia of Ocean Sciences, 3rd Edition. vol. 1, pp. 71-79, Elsevier. ISBN: 978-

618   0-12-813081-0, 2019.

619   O'Neill, L. W., Chelton, D. B., and Esbensen, S. K.: Observations of SST-induced perturbations of the

620   wind stress field over the Southern Ocean on seasonal timescales, Journal of Climate, 16, 2340-2354,

621   10.1175/2780.1, 2003.

622   Pineau-Guillou L., Ardhuin,F., Bouin,M.N.,Redelsperger,J.L.,Chapron,B., Bidlot, J. R., & Quilfen, Y.:

623   Strong winds in a coupled wave-atmosphere model during a North Atlantic storm event: evaluation

624   against observations. Quarterly Journal of the Royal Meteorological Society, 144(711), 317-332, 2018.

625   Polonichko, V.: Generation of Langmuir circulation for nonaligned wind stress and the Stokes drift, J.

626   Geophys. Res., 102, 15773-15780, https://doi.org/10.1029/97JC00460, 1997.

627   Powell, M. D., Vickery, P. J., and Reinhold, T. A.: Reduced drag coefficient for high wind speeds in

628   tropical cyclones, Nature, 422, 279-283, 10.1038/nature01481, 2003.

629   Qiao, F., Yuan, Y., Yang, Y., Zheng, Q., Xia, C., and Ma, J.: Wave‐induced mixing in the upper ocean:

630   Distribution and application to a global ocean circulation model, Geophysical Research Letters, 31,

631   http://dx.doi.org/10.1029/2004GL019824, 2004.

632   Renault, L., Arsouze, T., and Ballabrera-Poy, J.: On the Influence of the Current Feedback to the

633   Atmosphere on the Western Mediterranean Sea Dynamics, Journal of Geophysical Research-Oceans, 126,

634   10.1029/2020jc016664, 2021.

635   Renault, L., Molemaker, M. J., McWilliams, J. C., Shchepetkin, A. F., Lemarie, F., Chelton, D., Illig, S.,

636   and Hall, A.: Modulation of Wind Work by Oceanic Current Interaction with the Atmosphere, Journal of

637   Physical Oceanography, 46, 1685-1704, 10.1175/jpo-d-15-0232.1, 2016.

638   Reynolds, R. W., Smith, T. M., Liu, C., Chelton, D. B., Casey, K. S., and Schlax, M. G.: Daily High-

639   Resolution-Blended Analyses for Sea Surface Temperature, Journal of Climate, 20, 5473-5496,

640   http://dx.doi.org/10.1175/2007JCLI1824.1, 2007.

641   Saha, S., Moorthi, S., Pan, H., Wu, X., Wang, J., Nadiga, S., Tripp, P., Kistler, R., Woollen, J., and

642   Behringer, D.: The NCEP Climate Forecast System Reanalysis, Bulletin of the American Meteorological

643   Society, 91, 1015-1057, http://dx.doi.org/10.1175/2010BAMS3001.1, 2010.

644   Saha, S., Moorthi, S., Wu, X., Wang, J., Nadiga, S., Tripp, P., Behringer, D., Hou, Y., Chuang, H., and

645   Iredell, M. D.: The NCEP Climate Forecast System Version 2, Journal of Climate, 27, 2185-2208,

646   http://dx.doi.org/10.1175/JCLI-D-12-00823.1, 2014.

647   Sauvage, C., Lebeaupin Brossier, C., Bouin, M. N., & Ducrocq, V.: Characterization of the air-sea

648   exchange mechanisms during a Mediterranean heavy precipitation event using realistic sea state

649   modelling. Atmospheric Chemistry & Physics, 20(3), 2020.

650   Sharmar, V., and Markina, M.: Validation of global wind wave hindcasts using ERA5, MERRA2, ERA-

651   Interim and CFSRv2 reanalyzes, IOP Conference Series: Earth and Environmental Science, 606, 012056

652   (012059 pp.)-012056 (012059 pp.), 10.1088/1755-1315/606/1/012056, 2020.

653   Shimura, T., Mori, N., Takemi, T., et al.: Long term impacts of ocean wave-dependent roughness on

654   global climate systems. Journal of Geophysical Research: Oceans, 122(3),

655   https://doi.org/10.1002/2016JC012621, 2017.

656   Stopa, J. E., Ardhuin, F., Babanin, A. V., and Zieger, S.: Comparison and validation of physical wave

657   parameterizations in spectral wave models, Ocean Modelling, 103, 2-17,

658   http://dx.doi.org/10.1016/j.ocemod.2015.09.003, 2016.

659   Sweet, W., Fett, R., Kerling, J., and Laviolette, P.: Air-sea interaction effects in the lower troposphere

660   across the north wall of the Gulf Stream, Mon. Weather Rev., 109, 1042-1052, 10.1175/1520-

661   0493(1981)109<1042:Asieit>2.0.Co;2, 1981.

662   Takatama, K., and Schneider, N.: The Role of Back Pressure in the Atmospheric Response to Surface

663   Stress Induced by the Kuroshio, Journal of the Atmospheric Sciences, 74, 597-615, 10.1175/jas-d-16-

664   0149.1, 2017.

665   Taylor, P. K., and Yelland, M. J.: The Dependence of Sea Surface Roughness on the Height and Steepness

666   of the Waves, Journal of Physical Oceanography, 31, 572-590, http://dx.doi.org/10.1175/1520-

667   0485(2001)031%3C0572:TDOSSR%3E2.0.CO;2, 2001.

668   Terray, E. A., Donelan, M. A., Agrawal, Y. C., Drennan, W. M., Kahma, K. K., Williams, A. J., Hwang,

669   P. A., and Kitaigorodskii, S. A.: Estimates of Kinetic Energy Dissipation under Breaking Waves, Journal

670   of Physical Oceanography, 26, 792-807, http://dx.doi.org/10.1175/1520-

671   0485(1996)026%3C0792:EOKEDU%3E2.0.CO;2, 1996.

672   Tolman, H. L., and Chalikov, D. V.: Source Terms in a Third-Generation Wind Wave Model, Journal of

673   Physical Oceanography, 26, 2497-2518, http://dx.doi.org/10.1175/1520-

674   0485(1996)026%3C2497:STIATG%3E2.0.CO;2, 1996.

675 Van Roekel, L. P., Foxkemper, B., Sullivan, P. P., Hamlington, P. E., and Haney, S.: The form and

676 orientation of Langmuir cells for misaligned winds and waves, Journal of Geophysical Research, 117,

677 http://dx.doi.org/10.1029/2011JC007516, 2012.

678 Wang, L., and Xu, F.: Decadal variability and trends of oceanic barrier layers in tropical Pacific, Ocean

679 Dynamics, 68, 1155-1168, 10.1007/s10236-018-1191-3, 2018.

680 WAVEWATCH III Development Group.: User manual and system documentation of WAVEWATCH III

681 version 5.16, NOAA/NWS/NCEP/MMAB Technical Note 329, 326, 2016.

682 Wu, L., Staneva, J., Breivik, Ø., Rutgersson, A., Nurser, A. G., Clementi, E., and Madec, G.: Wave effects

683 on coastal upwelling and water level, Ocean Modelling, 140, 101405, 2019.

684 Wu, X., K. S. Moorthi, K. Okomoto, and H. L. Pan: Sea ice impacts on GFS forecasts at high latitudes,

685 Proceedings of the 85th AMS Annual Meeting, 8th Conference on Polar Meteorology and Oceanography,

686 San Diego, CA, 2005.

687 Zieger, S., Babanin, A. V., Rogers, W. E., and Young, I. R.: Observation-based source terms in the third-

688 generation wave model WAVEWATCH, Ocean Modelling, 96, 2-25,

689 http://dx.doi.org/10.1016/j.ocemod.2015.07.014, 2015.

Table 1. List of numerical experiments: setups different from CTRL are marked with bold

Experiments	Physical Process/Parameterization		
	Langmuir Cell with Stokes-Coriolis Force and Entrainment	Roughness (Charnock Parameter)	Relative Velocity in Flux
CTRL	Off	Off	Off
VR12-AL-SC-EN	**Eqn. 1-6, 8-10**	Off	Off
Z0-M04	Off	$\mathbf{C_{ch}}$ **from Eqn. 16, 17**	Off
FLUX	Off	Off	$\mathbf{\Delta\vec{V}}$ **from Eqn. 14**
ALL	**Eqn. 1-6, 8-10**	$\mathbf{C_{ch}}$ **from Eqn. 16, 17**	$\mathbf{\Delta\vec{V}}$ **from Eqn. 14**

Table 2. The 53-day mean bias with standard deviation (STD) and RMSE for WSP10 and SWH compared with NDBC buoy observation: the bias is calculated as simulation minus NDBC.

Boreal Winter WSP10	Bias with STD	RMSE
CTRL	0.16±1.23	1.24
VR12-AL-SC-EN	0.01±1.12	1.12
Z0-M04	-0.01±1.07	1.07
FLUX	0.39±1.20	1.26
ALL	0.07±1.04	1.04
Boreal Winter SWH	**Bias with STD**	**RMSE**
CTRL	0.21±0.38	0.44
VR12-AL-SC-EN	0.14±0.35	0.37
Z0-M04	0.10±0.30	0.32
FLUX	0.24±0.34	0.42
ALL	0.12±0.34	0.36
Boreal Summer WSP10	**Bias with STD**	**RMSE**
CTRL	0.15±1.23	1.24
VR12-AL-SC-EN	-0.03±1.22	1.22
Z0-M04	-0.04±1.21	1.21
FLUX	-0.22±1.18	1.20
ALL	-0.17±1.14	1.15
Boreal Summer SWH	**Bias with STD**	**RMSE**
CTRL	0.28±0.25	0.38
VR12-AL-SC-EN	0.19±0.24	0.30
Z0-M04	0.22±0.26	0.34
FLUX	0.14±0.25	0.29
ALL	0.12±0.21	0.24
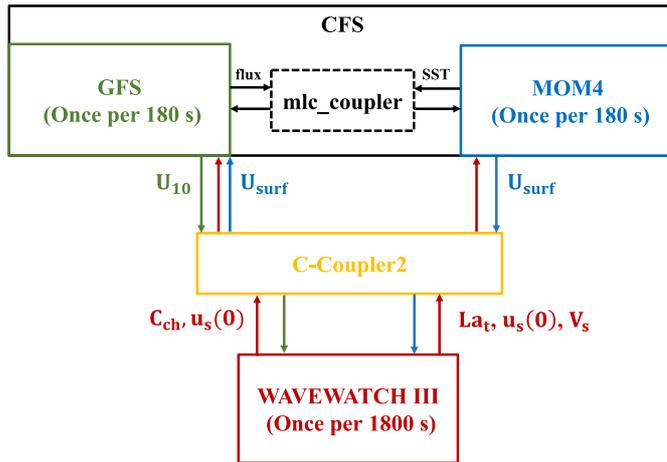
Figure 1. A schematic diagram of the atmosphere-ocean-wave coupled modeling system. The arrows indicate the coupled variables that are passed between the model components. In the diagram, C_{ch}, La_t, $u_s(0)$, V_s, U_{10}, and U_{surf} are Charnock parameter (red arrows), turbulent Langmuir number (red arrows), surface Stokes drift velocity (red arrows), Stokes transport (red arrows), 10-m wind (green arrows) and surface current (blue arrows), respectively.
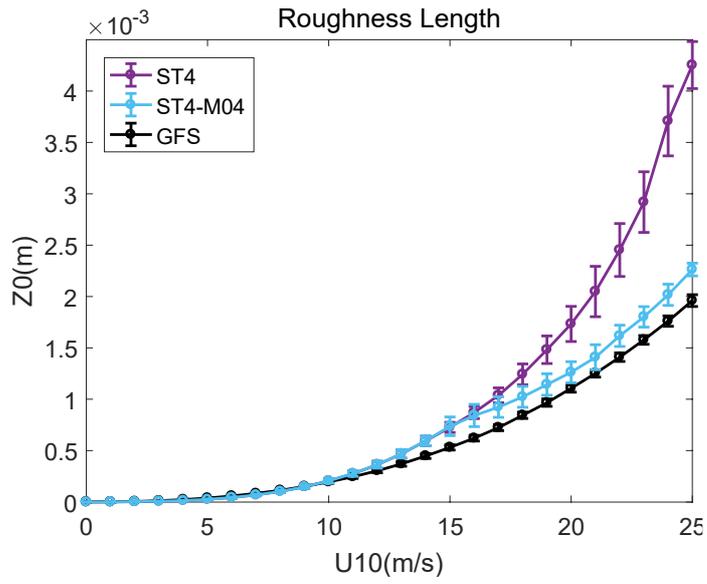
Figure 2. Relationships between momentum roughness length z_0 (m) in the coupled system and 10-m wind speed (m/s); error bars indicate twice the standard deviations for each point.
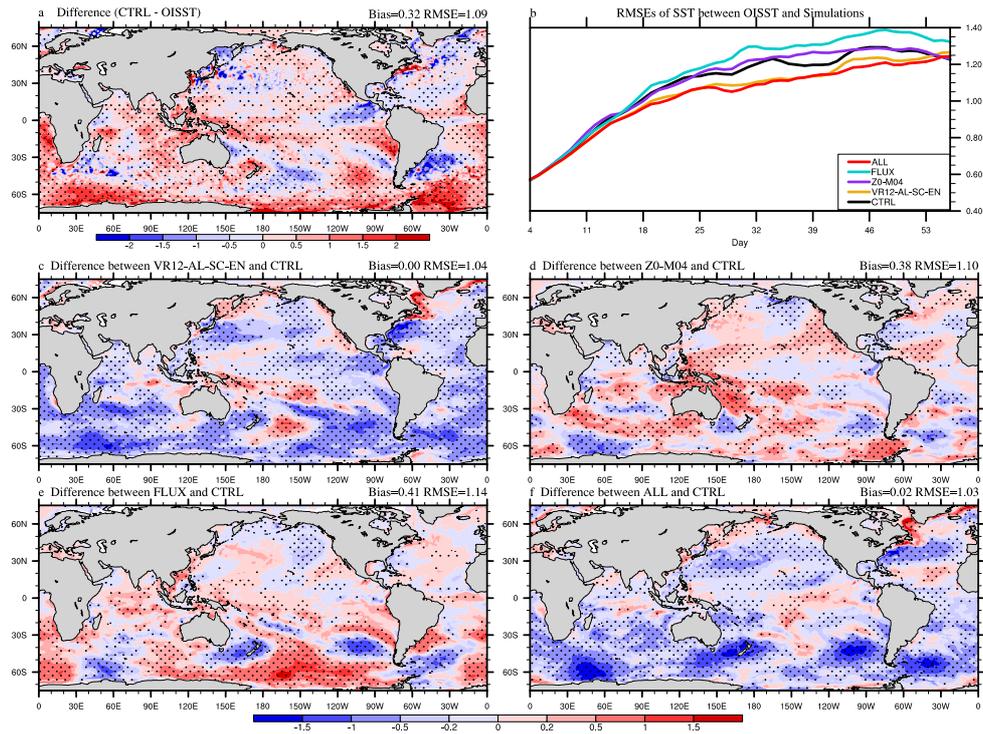
Figure 3. The 53-day average SST (℃) bias in CTRL (a; CTRL minus OISST), the time series of global-averaged RMSE (b), and the differences between VR12-AL-SC-EN (c)/Z0-M04 (d)/ FLUX (e)/ ALL (f) and CTRL in Jan-Feb, 2017 (VR12-AL-SC-EN/Z0-M04/FLUX/ALL minus CTRL). The first 3-day simulation is discarded. The dotted areas are statistically significant at 95% confidence level.
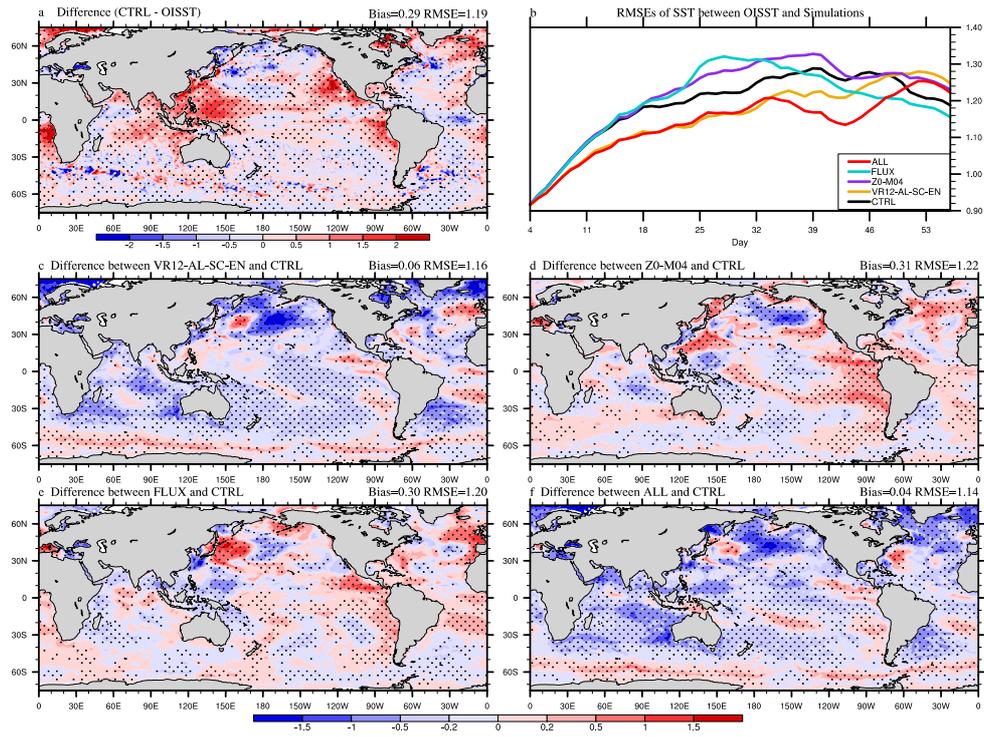
Figure 4. The same as Figure 3 but for Aug-Sep, 2018.
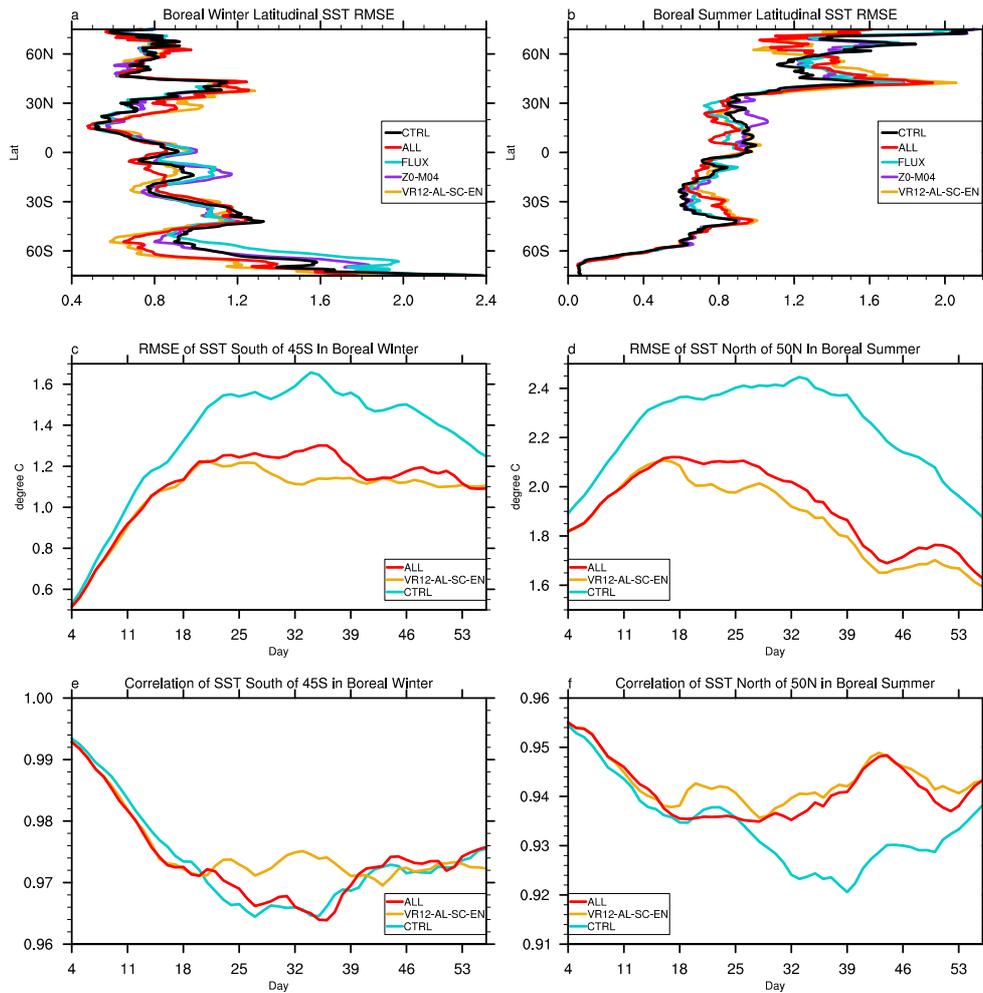
Figure 5. The 53-day averaged latitudinal distribution of SST root mean square errors (RMSE), time series of domain-averaged SST RMSE and correlation coefficient: **a/b** the latitudinal RMSE in boreal winter/summer compared with OISST, **c/d** the time series of domain-averaged (0-360°E, 45-78°S/50-78°N) SST RMSE in boreal winter/summer, **e/f** the time series of domain-averaged (0-360°E, 45-78°S/50-78°N) SST correlation coefficient in boreal winter/summer; differences of RMSE and correlation coefficient time series between VR12-AL-SC-EN/ALL and CTRL are statistically significant at 99% confidence level, except those in Fig. e.
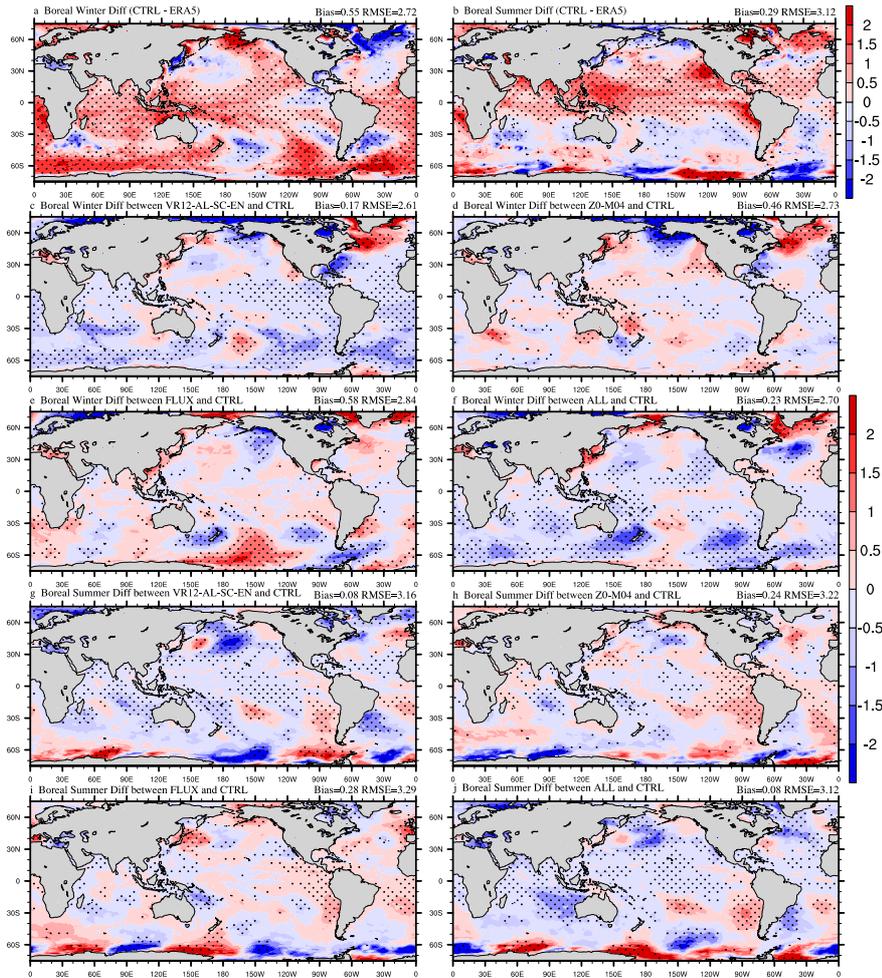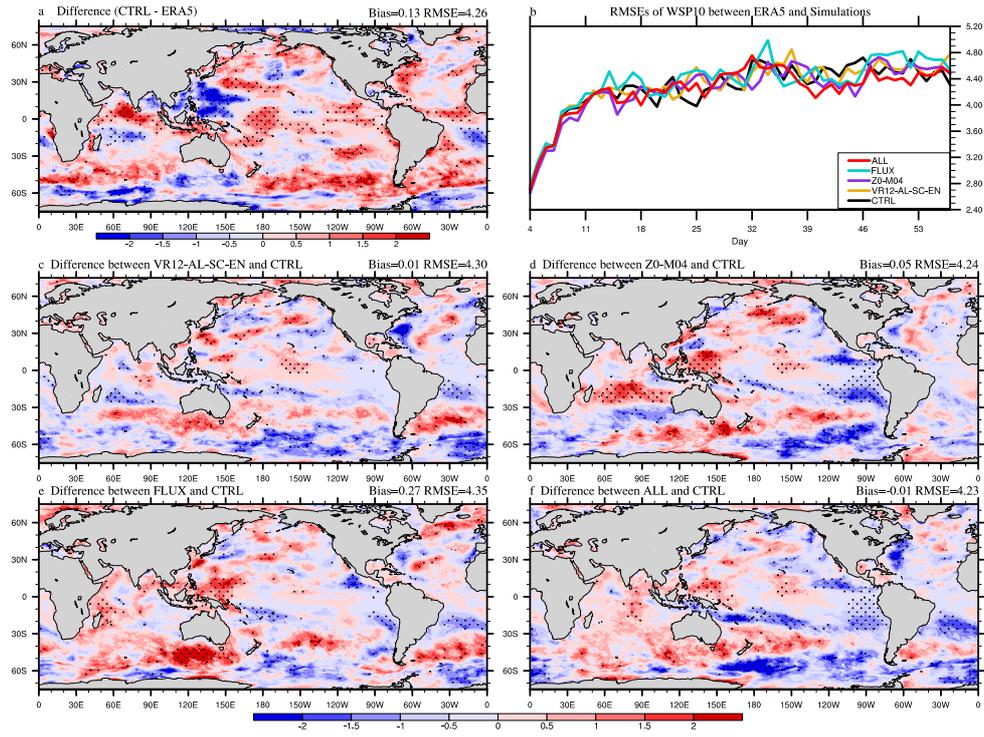
Figure 6. The 53-day average T02 (℃) bias in CTRL (a&b; CTRL minus ERA5), and the differences between VR12-AL-SC-EN (c&g)/Z0-M04 (d&h)/ FLUX (e&i)/ ALL (f&j) and CTRL (VR12-AL-SC-EN/Z0-M04/FLUX/ALL minus CTRL). The first 3-day simulation is discarded. The dotted areas are statistically significant at 95% confidence level. a/c/d/e/f are for Jan-Feb, 2017, and b/g/h/i/j are for Aug-Sep, 2018.
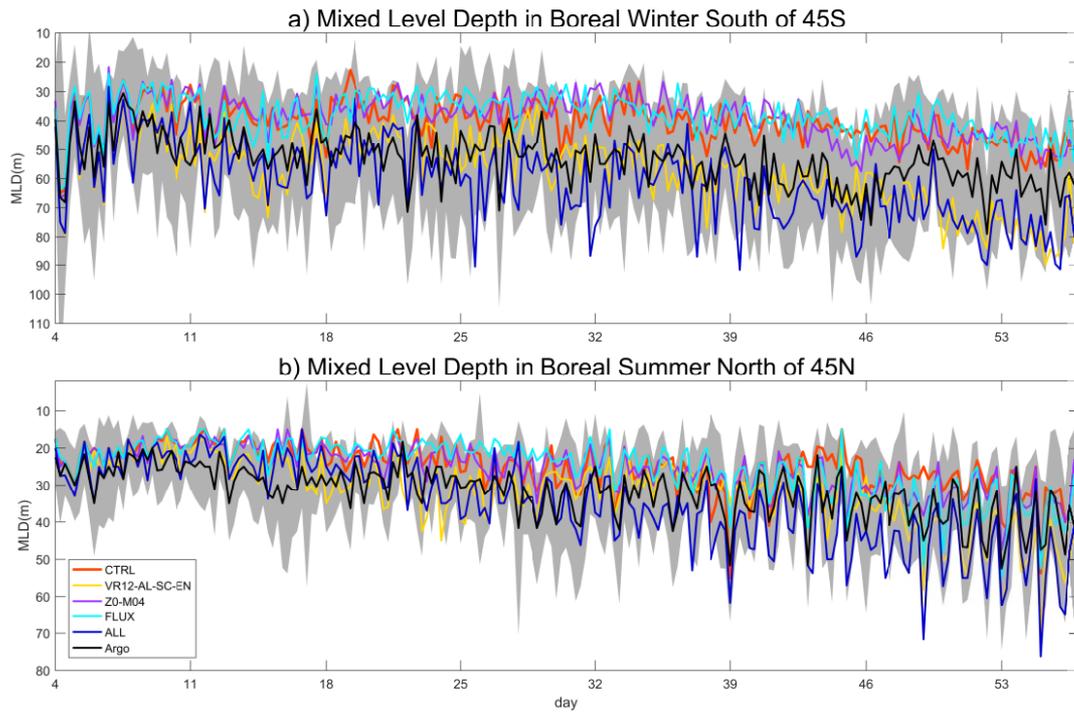
Figure 7. The 53-day time series of domain-averaged (0-360°E, 45-78°S/N) mixed layer depth (MLD; m) in boreal winter/summer: the difference between CTRL and VR12-AL-SC-EN/ALL passes the student's t-test at 99% confidence level; the time intervals are 6 hours; shaded areas indicate twice the standard deviations for Argo.
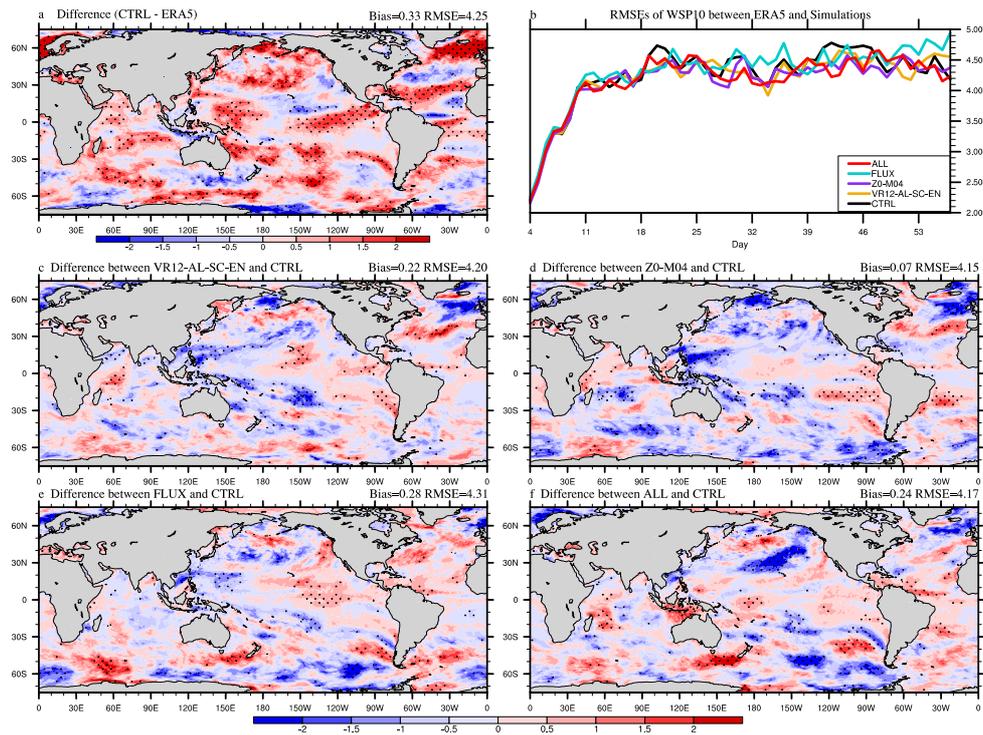
Figure 8. The 53-day average WSP10 (m/s) bias in CTRL (a; CTRL minus ERA5), the time series of global-averaged RMSE (b), and the differences between VR12-AL-SC-EN (c)/Z0-M04 (d)/ FLUX (e)/ ALL (f) and CTRL in Jan-Feb, 2017 (VR12-AL-SC-EN/Z0-M04/FLUX/ALL minus CTRL). The first 3-day simulation is discarded. The dotted areas are statistically significant at 95% confidence level.

Figure 9. The same as Figure 8 but for Aug-Sep, 2018.
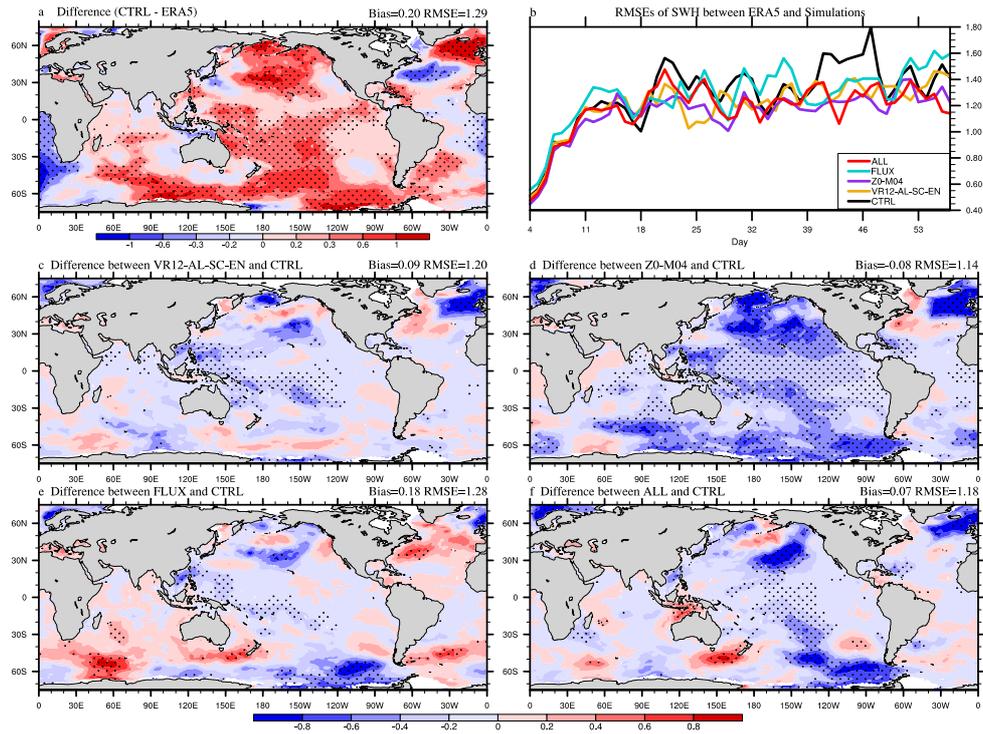
Figure 10. The 53-day average SWH (m) bias in CTRL (a; CTRL minus ERA5), the time series of global-averaged RMSE (b), and the differences between VR12-AL-SC-EN (c)/Z0-M04 (d)/ FLUX (e)/ ALL (f) and CTRL in Jan-Feb, 2017 (VR12-AL-SC-EN/Z0-M04/FLUX/ALL minus CTRL). The first 3-day simulation is discarded. The dotted areas are statistically significant at 95% confidence level.
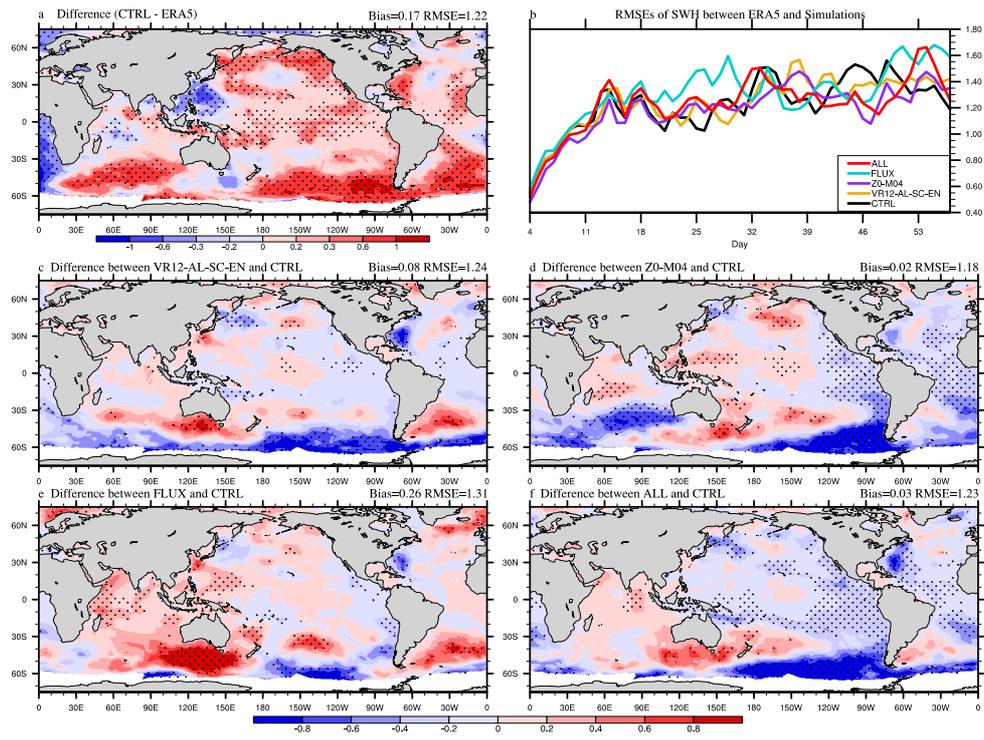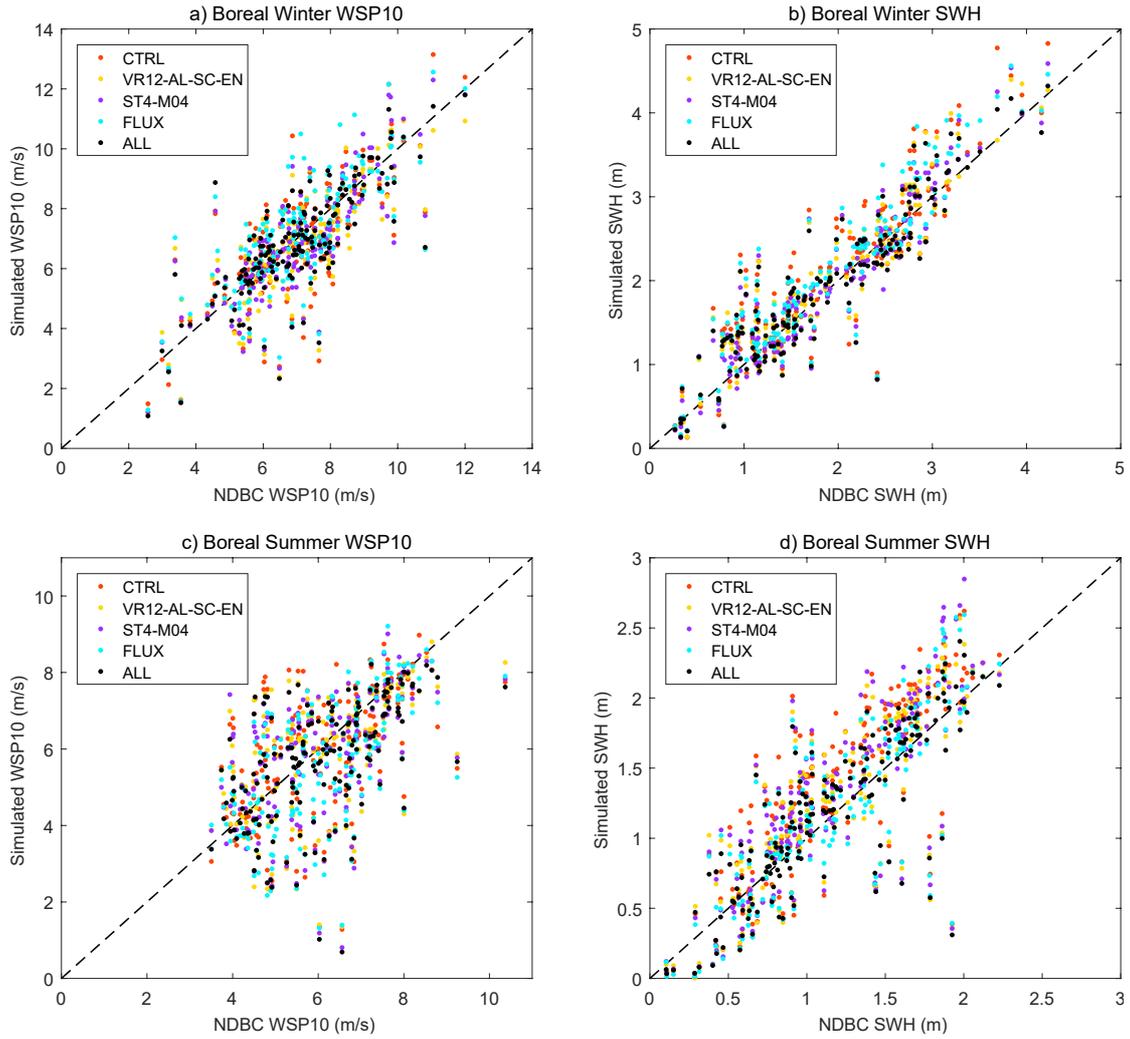
Figure 11. The same as Figure 10 but for Aug-Sep, 2018.

Figure 12. Scatter plots of simulated WSP10/SWH (y-axis) vs buoy WSP10/SWH (x-axis): (a) the WSP10 in Jan-Feb, 2017, (b) the SWH in Jan-Feb, 2017, (c) the WSP10 in Aug-Sep, 2018, and (d) the SWH in Aug-Sep, 2018. The dotted line is y=x. The corresponding mean biases with standard deviations and RMSEs for every experiment are shown in Table 2.